

Control of a Permanent Magnet Synchronous Machine for use in an Active Suspension System, with a Magnetic Lead Screw

E. Jensen, J. Seegert, P. Sørensen, R. Kæseler, T. Nielsen

Department of Materials and Production, Aalborg University
Fibigerstraede 16, DK-9220 Aalborg East, Denmark

Email: { [emje13](mailto:emje13@student.aau.dk), [jseege16](mailto:jseege16@student.aau.dk), [pjsa13](mailto:pjsa13@student.aau.dk), [rkasel13](mailto:rkasel13@student.aau.dk), [tornie13](mailto:tornie13@student.aau.dk) } @student.aau.dk

Web page: <http://www.mechman.m-tech.aau.dk/>

Abstract

This paper investigates how a Permanent Magnet Synchronous Machine (PMSM) can be used in combination with a Magnetic Lead Screw (MLS) as an active automotive shock absorber. The PMSM utilizes a hollow rotor, encircled by permanent magnets on the outside with which the stator field interacts. The interior of the hollow rotor is equipped with helical shaped magnets, facilitating rotation relative to the MLS translator. After assembly of the PMSM, test are performed to evaluate parameters for a mathematical model. The model is validated through various tests, and a field oriented control scheme is developed. Furthermore, vehicle dynamics are investigated to estimate the conditions the shock absorbing unit will be subjected to.

Keywords: Active Suspension, Permanent Magnet Synchronous Machine, Magnetic Lead Screw

1. Introduction

The automotive industry have had greater focus on suspension systems in recent years, and three general terms have been made to distinguish between them: Passive-, active- and semi-active suspension systems. Traditionally, the passive system consists of a steel spring and a viscous damper, providing suspension with constant damping. This is still the most commonly used system implemented in cars today, but newer and more advanced systems are closing this gap. Active systems inputs power to control roll, pitch, and heave, whereas semi-active only changes the suspensions energy dissipation. General Motors have developed a semi-active system [1], while Mercedes [2] and Bose [3] have made active systems. The success of these are highly dependent on weight and cost, which leads to continuous interest in the development, why Aalborg University (AAU) have researched these suspension systems.

Previous work from AAU investigated a Magnetic Lead Screw's (MLS) efficiency and ability to function as a wave energy converter, documented in [4] and [5]. It was outlined in [4] that the MLS has a high efficiency of more than 90 % due to the reduction of contact elements. In [6] a single MLS was implemented in a Vehicle Test Platform (VTP) in conjunction with a Permanent Magnet

Synchronous Machine (PMSM) and an air spring, which combined constituted the new shock absorber design. A PMSM has the advantage of being compact, making it ideal in this regard due to space limitations. The PMSM can work as both generator and motor at high efficiencies, which is essential for an energy efficient system. In order to fully explore the potential of shock absorbers in vehicles, a VTP with four shock absorbers are of interest. One native front suspension unit in a VW Passat B5 has already been replaced with this new system, why this paper assembles and examines a second suspension unit for implementation in the VTP. A 3D representation of the completed assembly is displayed on Fig. 1.

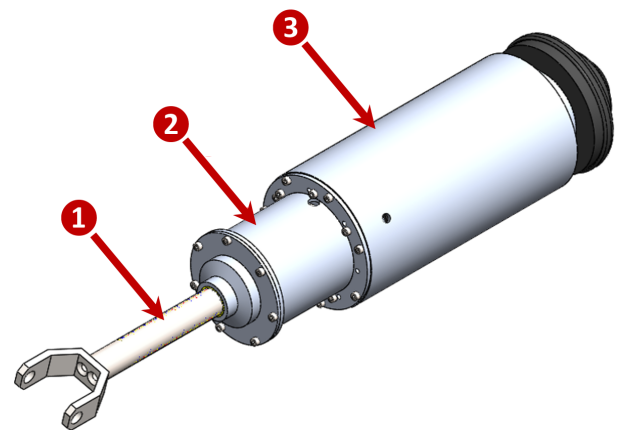


Fig. 1 3D illustration of an assembled shock absorber [6].

2. Manufacturing

The construction of the shock absorber included the assembly of three major parts; the MLS (1), the PMSM (2) and an air spring (3). The PMSM stator is shown in Fig. 2. To prevent the stator iron from damaging the windings (4), mylar paper (5) is placed in each slot, and a fiber cloth (6) at the ends of the stator cross section. Finally, glass fiber sticks (7) is placed in the slots as an enclosure, keeping the windings in place.

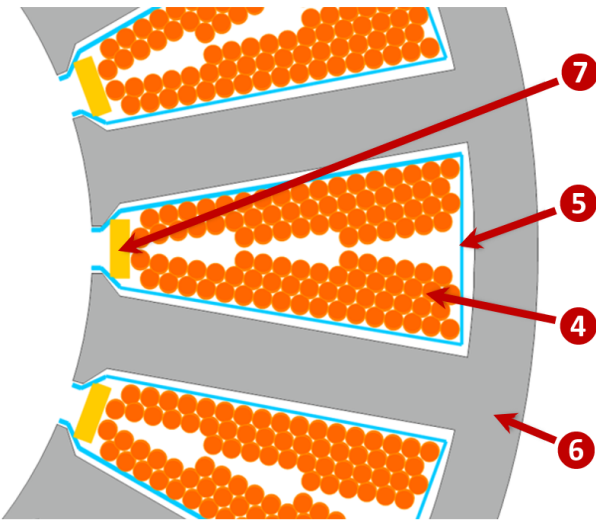


Fig. 2 Cross sectional illustration of the stator.

After assembly, PMSM stator is tested with a 1000 V megger, to ensure the integrity of the field windings. The windings are connected together to form three phases as indicated on Fig. 3. The three phases are connected together in a star point, long wires for connections are soldered and exposed areas are isolated with heat shrink tubing. Finally, waxed cotton string is applied to tie down loose wires.

The assembly of the PMSM rotor, the MLS rotor and the MLS translator is initialized by gluing permanent neodymium magnets onto each component. The PMSM utilizes a hollow rotor design with 20 magnetic poles mounted on the outside perimeter in a shifting pattern. Rectangular shaped magnets are used, whereas the MLS rotor and translator utilizes helically shaped magnets instead. To obtain an optimal flux field without compromising the manufacturing complexity, the neodymium magnets have been magnetized in three different directions. They are then arranged in a spiralling pattern throughout the translator shaft, following the schematic of a Halbach array illustrated on Fig. 4. This pattern is

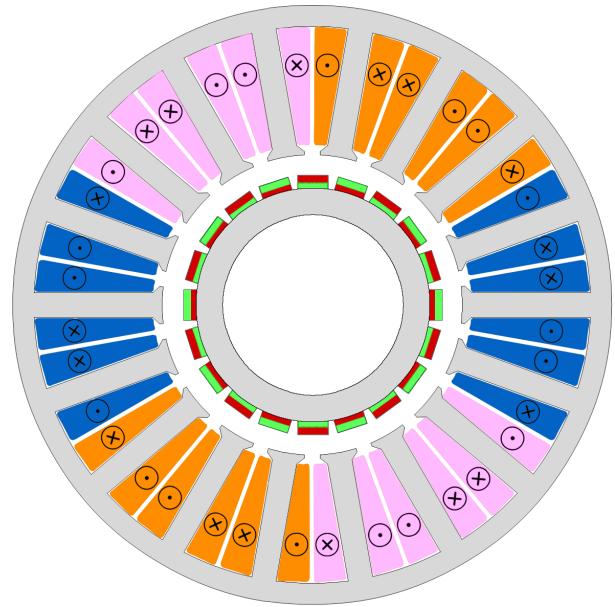


Fig. 3 Illustration of field windings.

chosen to minimize iron losses by concentrating flux towards away from the back iron, into the airgap.



Fig. 4 Halbach schematic for optimal flux density.

The final preparations, before the complete lead screw is assembled, includes sealing the air gaps between each magnet with an epoxy based filler. This serves to reinforce the structure, locking the magnets in position during the final milling process. Here the outer diameter is reduced to in order to smoothen the surface and prepare it for installation within the rotor. A SolidWorks drawing of the assembled MLS is shown on Fig. 5.

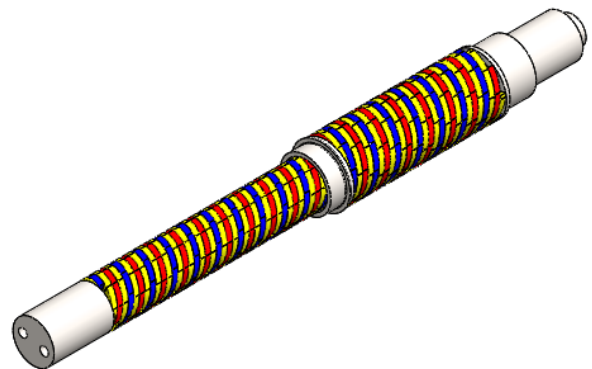


Fig. 5 SolidWorks drawing of MLS translator and rotor [6].

3. Mathematical Model

The entire suspension system can advantageously be divided into smaller segments, which can then be mathematically described individually. The PMSM represent one of these subsystems, why an electrical equivalent circuit of the is established. It consists of three phases, each with an inductor, a resistor and a counter-electromotive force (back-EMF) connected in series. The phases are joined in a star formation as illustrated on Fig. 6. The back-EMF is the voltage induced in the windings, by the permanent magnets, as the rotor spins.

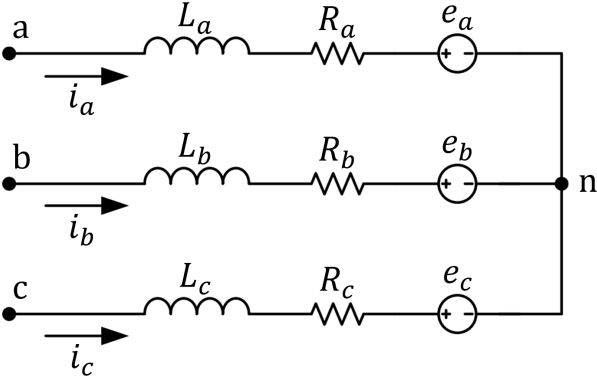


Fig. 6 Equivalent circuit of the PMSM

A set of voltage equations can be derived for the stationary abc-reference frame, based upon the equivalent diagram. The matrix form of these are shown in Eq. 1.

$$\begin{bmatrix} u_a \\ u_b \\ u_c \end{bmatrix} = \begin{bmatrix} L_a & L_{ba} & L_{ca} \\ L_{ba} & L_b & L_{cb} \\ L_{ca} & L_{cb} & L_c \end{bmatrix} \frac{d}{dt} \begin{bmatrix} i_a \\ i_b \\ i_c \end{bmatrix} + \begin{bmatrix} R_a & 0 & 0 \\ 0 & R_b & 0 \\ 0 & 0 & R_c \end{bmatrix} \begin{bmatrix} i_a \\ i_b \\ i_c \end{bmatrix} + \begin{bmatrix} e_a \\ e_b \\ e_c \end{bmatrix} \quad (1)$$

The phase resistors may have small asymmetries due to the manual manufacturing, but they are assumed negligible. The inductors may also deviate from each other, but this is neglected as well. The assumption of equal mutual inductance are also made, which is shown in Eq. 2.

$$\begin{aligned} R &= R_a = R_b = R_c \\ L &= L_a = L_b = L_c \\ M &= L_{ab} = L_{bc} = L_{ca} \end{aligned} \quad (2)$$

Since the star connection must follow Kirchhoff's current law, Eq. 3 must also apply for the system.

$$i_a + i_b + i_c = 0 \quad Mi_b + Mi_c = -Mi_a \quad (3)$$

This simplifies Eq. 1 to Eq. 4.

$$\begin{bmatrix} u_a \\ u_b \\ u_c \end{bmatrix} = \begin{bmatrix} L - M & 0 & 0 \\ 0 & L - M & 0 \\ 0 & 0 & L - M \end{bmatrix} \frac{d}{dt} \begin{bmatrix} i_a \\ i_b \\ i_c \end{bmatrix} + \begin{bmatrix} R & 0 & 0 \\ 0 & R & 0 \\ 0 & 0 & R \end{bmatrix} \begin{bmatrix} i_a \\ i_b \\ i_c \end{bmatrix} + \begin{bmatrix} \epsilon_a \\ \epsilon_b \\ \epsilon_c \end{bmatrix} \quad (4)$$

This phase plane representation can be simplified further. By transforming the equations into a stator fixed α, β coordinate system, and then into a rotor fixed d, q coordinate system, some mathematical simplifications emerge. AC quantities become DC providing a static reference frame for the controller to operate on. The stator fixed coordinate system is obtained by the Clarke transformation and the rotor fixed coordinate system is obtained with the Park transformation. The Clarke transformation matrix is shown in Eq. 5.

$$\begin{bmatrix} x_\alpha \\ x_\beta \end{bmatrix} = \frac{2}{3} \begin{bmatrix} 1 & -\frac{1}{2} & -\frac{1}{2} \\ 0 & \frac{\sqrt{3}}{2} & -\frac{\sqrt{3}}{2} \end{bmatrix} \begin{bmatrix} x_a \\ x_b \\ x_c \end{bmatrix} \quad (5)$$

The Park transformation matrix is shown in Eq. 6.

$$\begin{bmatrix} x_d \\ x_q \end{bmatrix} = \begin{bmatrix} \cos(\theta_e) & \sin(\theta_e) \\ -\sin(\theta_e) & \cos(\theta_e) \end{bmatrix} \begin{bmatrix} x_\alpha \\ x_\beta \end{bmatrix} \quad (6)$$

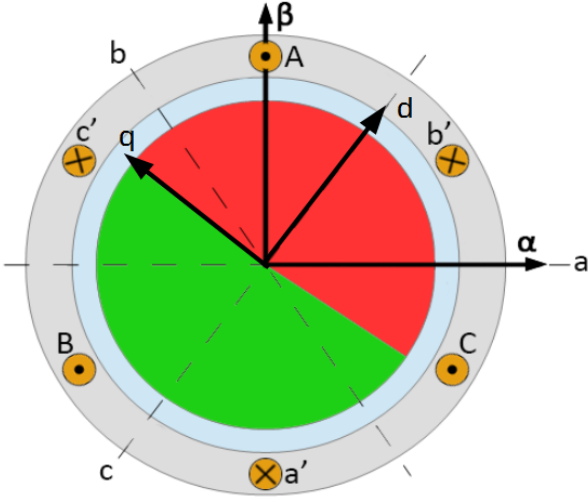


Fig. 7 Illustration of different coordinate systems.

The rotor fixed voltage equations can now be rewritten as Eq. 7. Here ω_e represents the angular velocity of the electric field, while λ_{pm} denotes the flux linkage in the air gap, generated the permanent magnets.

$$\begin{aligned} u_d &= Ri_d + L \frac{di_d}{dt} - \omega_e Li_q \\ u_q &= Ri_q + L \frac{di_q}{dt} + \omega_e (Li_d + \lambda_{pm}) \end{aligned} \quad (7)$$

Torque can be calculated using Eq. 8, if q- and d-axis inductances are assumed to be identical. In the case of surface mounted permanent magnets, this assumption is a fair approximation. The number of magnetic poles on the rotor is represented with p .

$$\tau_e = \frac{3p}{4} \lambda_{pm} i_q \quad (8)$$

From Eq. 8 it can be seen that torque is proportional to the q-axis current. The d-axis current is aligned with the rotors magnetic pole and provides no torque. Therefore, the d-axis current should be controlled to 0, as it only contributes additional iron and copper losses.

The angular velocity ω_m of the PMSM can be determined using newtons 2nd law for rotating bodies. This is an ordinary differential equation as shown in Eq. 9. Here J_m is mass moment of inertia, B_m is viscous friction, τ_{df} is dry friction and load torque is τ_L .

$$\tau_e = J_m \frac{2 d\omega_e}{p dt} + \frac{2}{p} B_m \omega_m + \tau_{df} + \tau_L \quad (9)$$

The Variable Frequency Drive (VFD) primarily consists of two subsystems; the inverter and the micro controller. The purpose of the inverter is to distribute voltage from the DC-bus across each phase using the six internal switches illustrated on Fig. 8. The micro controller generates the Pulse-Width Modulation (PWM) signals used to control the switches during operation. The duty cycles are calculated by comparing the modulation signal with a triangular carrier wave with a predefined frequency. Simplifications regarding the modelling includes the assumption of infinitely fast transistor switches, no dead time when switching and a constant DC-bus value.

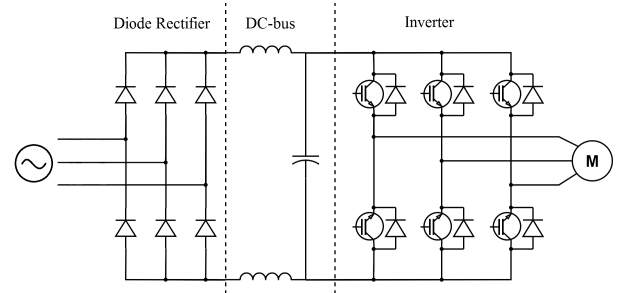


Fig. 8 Inverter circuit diagram.

The modulation signal is generated by space vector modulation. This modulation technique relies on switching between different vectors as seen on Fig. 9. The reference vector is shown by U_s . Fixed vectors are eg. V_{100} where the three subscripts indicates phase A,B and C respectively. 1 indicates the switch is connected to the high leg of the DC bus and 0 the low leg. In addition to the vectors shown, two zero vectors (000) and (111) exist. On the zero vectors, all three phases have the same potential making the line to line potential 0. To realise the reference vector, the modulator would switch between two active vectors and a zero vector. The time spent on each of the active vectors is determined the by the angle of the reference vector, while the time spent on the zero vector is determined by the amplitude of the reference vector.

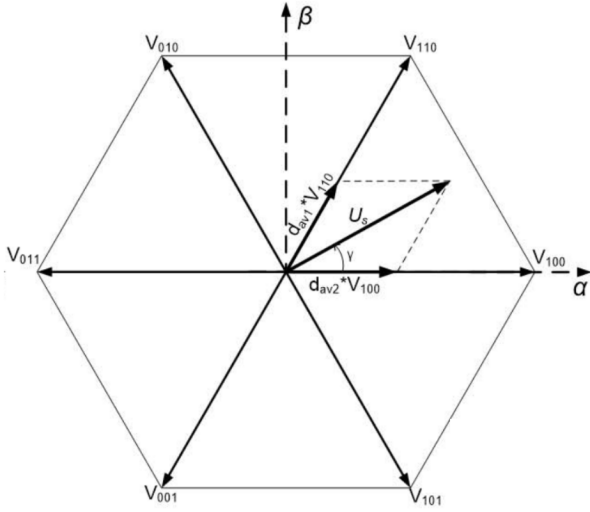


Fig. 9 Space vector diagram from [7].

4. Parameters

For accurate modelling and control of the PMSM, the electromechanical characteristics must be determined. This was done through various tests, and the results is displayed in Tab. I.

Parameter	Symbol	Value	Unit
Phase resistance	R	0.41	$[\Omega]$
Phase inductance	L	$1.13 \cdot 10^{-3}$	$[H]$
Back-EMF constant	λ_{pm}	$2.97 \cdot 10^{-2}$	$[V \cdot s/rad]$
Torque constant	K_T	0.4455	$[Nm/A]$
Iron and friction losses	B	$2.9 \cdot 10^{-3}$	$[Nm \cdot s/rad]$

Tab. I Measured PMSM parameters.

The phase resistance was found using Ohm's law $R = U/I$. Constant voltage was applied across one phase, while the current was measured. This process was repeated on the other two phases after which an average was calculated.

The inductance is determined by method of instantaneous flux linkage [8]. The rotor shaft is locked in place with a steel plate throughout the test, in order to exclude any influence from back-EMF. A volt step is given while measuring voltage and current. One phase is connected to the positive terminal, and the other two to the negative. The instantaneous flux linkage is given by Eq. 10 and the inductance by Eq. 11. The equivalent inductance for a single phase is desired, hence the $\frac{2}{3}$ in Eq. 11.

$$\lambda(t) = \int_{t_0}^t U(t) - Ri(t)dt \quad (10)$$

$$L = \frac{2\lambda(t)}{3i(t)} \quad (11)$$

In order to determine the back-EMF constant, a hand drill is connected to the rotor shaft to bring it up to speed. This induces a voltage in the PMSM coils which is measured with an oscilloscope. By measuring the line-to-line voltages together with the electrical frequency, the back-EMF constant is calculated using Eq. 12. Conversion factors $\sqrt{2}$ and $\sqrt{3}$ are used to express the back EMF constant in units $[V_{peak}/(rad/s)]$.

$$\lambda_{pm} = \frac{\sqrt{2}u_{l-l,rms}}{\sqrt{3}\omega_e} \quad (12)$$

Finally, the power loss due to viscous friction and iron losses (hysteresis and eddy current losses) are determined. Since they are difficult to separate, they are expressed together as a single coefficient B_m , calculated with Eq. 13. In this test, the mechanical velocity ω_m of the load motor is increased in intervals of 100 RPM. Meanwhile, the resisting torque τ_{vf} from the PMSM is measured with the transducer. The setup for tests and validation is displayed on Fig. 21.

$$B_m = \frac{\tau_{vf}}{\omega_m} \quad (13)$$

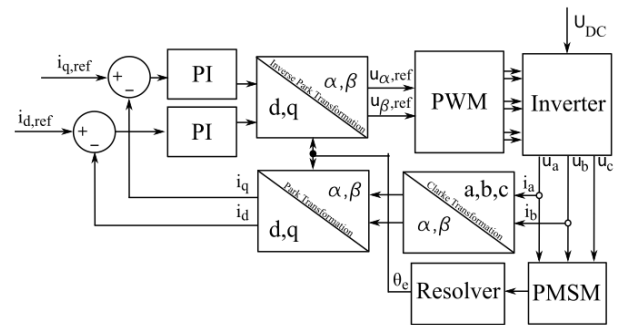


Fig. 10 Block diagram of field oriented control.

5. Test and validation

Before a controller can be designed, a validation of the model is performed to ensure it replicates the real system. Closed loop tests with a previously designed PI controller [6] is conducted to analyze the dynamic response. Fig. 11 displays the response from a 2 Ampere q-axis current step, which are nearly identical both in amplitude and transient response.

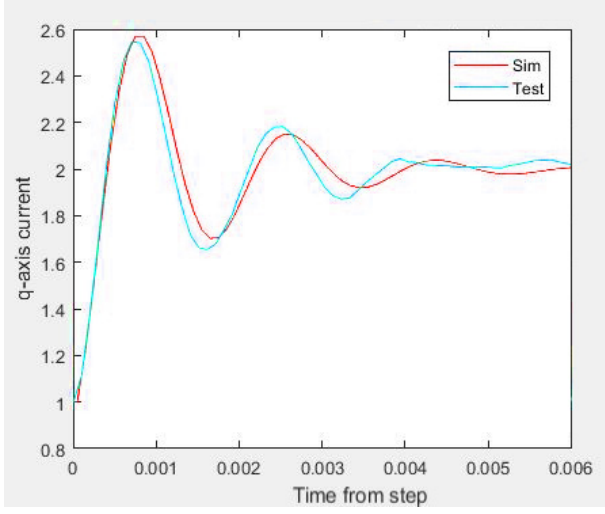


Fig. 11 Step response comparison between the nonlinear model and measured data.

Some open loop experiments are conducted as well, but these revealed inconsistencies between the model and the test data. Specifically, the cross-couplings showed significantly different behaviour in simulation and test data. To examine the couplings closer, a Relative Gain Array (RGA) analysis is conducted on the linearized model.

6. Linearisation

Transfer functions are derived through a linearization by Taylor series approximation. The following linearization point is used:

$$\omega_{e,0} = 200 \frac{\text{rad}}{\text{s}} \quad , \quad i_{q,0} = 2\text{A} \quad , \quad i_{d,0} = 0.6\text{A} \quad (14)$$

Yielding linearisation coefficients:

$$\begin{aligned} K_d &= K_q = \omega_{e,0}L = 0.1242 \\ K_{wd} &= i_{q,0}L = 0 \\ K_{wq} &= i_{d,0}L = 0.0023 \end{aligned} \quad (15)$$

Applying the coefficients to the voltage and mechanical equations yields the following state space model:

$$\begin{aligned} \frac{d}{dt} \begin{bmatrix} i_d \\ i_q \\ \omega_e \end{bmatrix} &= \overbrace{\begin{bmatrix} \frac{-R}{L_d} & \frac{K_q}{L_d} & \frac{K_{wq}}{L_d} \\ \frac{-K_d}{L_q} & \frac{-R}{L_q} & \frac{-K_{wd} - \lambda_{pm}}{L_q} \\ 0 & \frac{3P^2 \lambda_{pm}}{2J} & \frac{-B_m}{J} \end{bmatrix}}^A \overbrace{\begin{bmatrix} i_d \\ i_q \\ \omega_e \end{bmatrix}}^B \\ &+ \begin{bmatrix} \frac{1}{L_d} & 0 & 0 \\ 0 & \frac{1}{L_q} & 0 \\ 0 & 0 & -\frac{P}{J} \end{bmatrix} \begin{bmatrix} U_d \\ U_q \\ \tau_L \end{bmatrix} \\ \begin{bmatrix} i_d \\ i_q \\ \omega_m \end{bmatrix} &= \overbrace{\begin{bmatrix} 1 & 0 & 0 \\ 0 & 1 & 0 \\ 0 & 0 & \frac{1}{P} \end{bmatrix}}^C \begin{bmatrix} i_d \\ i_q \\ \omega_e \end{bmatrix} \end{aligned} \quad (16)$$

This can be transformed to transfer functions by:

$$G(s) = C(sI - A)^{-1}B \quad (17)$$

yielding a 3x3 system. As it is desired to control the currents i_q and i_d with the voltages, U_q and U_d respectively, the transfer functions concerning these inputs and outputs are all considered, as follows:

$$\begin{bmatrix} i_d \\ i_q \end{bmatrix} = \begin{bmatrix} G(1,1) & G(1,2) \\ G(2,1) & G(2,2) \end{bmatrix} \begin{bmatrix} U_d \\ U_q \end{bmatrix} \quad (18)$$

The RGA analysis investigates, as the name suggests, the relative gain between inputs and output, and specifically the cross couplings, i.e. what influence voltage U_q will have on i_d and U_d on i_q . As this is the subject of the analysis only the transfer functions dependent on the voltages should be included. The RGA elements can therefore be calculated as:

$$\text{RGA}(H) = \begin{bmatrix} \lambda_{11} & \lambda_{12} \\ \lambda_{21} & \lambda_{22} \end{bmatrix} = \begin{bmatrix} \lambda_{11} & 1 - \lambda_{11} \\ 1 - \lambda_{11} & \lambda_{11} \end{bmatrix} \quad (19)$$

$$\lambda_{11} = \frac{1}{1 - \frac{h_{12}h_{21}}{h_{11}h_{22}}}$$

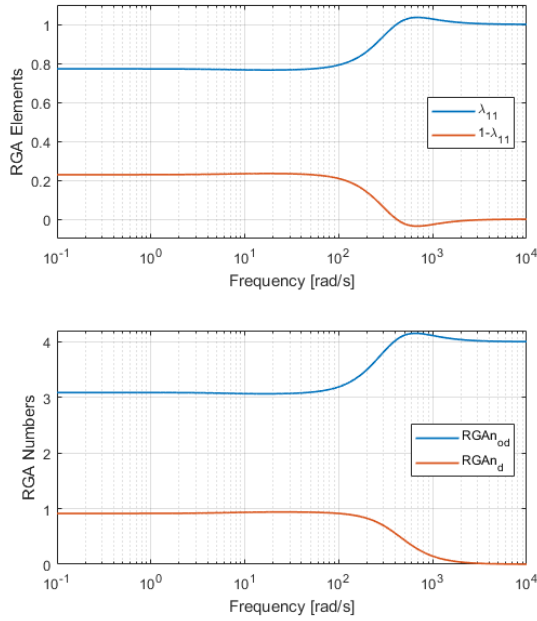


Fig. 12 RGA numbers and elements.

Sweeping through frequencies from 10^{-1} to 10^4 yields the RGA elements and numbers on Fig. 12. A fully decoupled system is $RGA(H) = I$, meaning $\lambda = 1$ and $1 - \lambda = 0$. The element values can be seen to be approximately 0.8 and 0.2 respectively, which indicates cross couplings between inputs and outputs, which was also proven by a open loop voltage step, shown on Fig. 13.

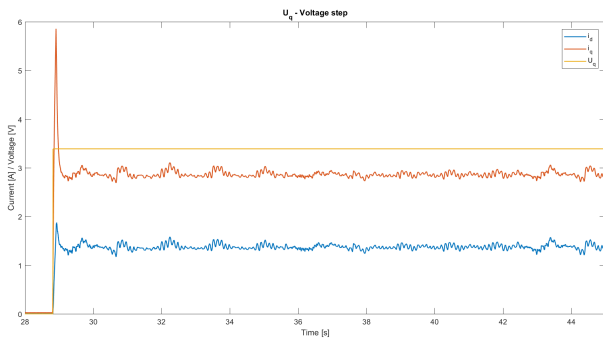


Fig. 13 Voltage step with current responses.

The linear model was compared to measured data with a voltage step of 28 V, resulting in the current response shown on Fig. 14 and the velocity response on Fig. 15. This was an insufficient response, but a gain of 1/3 of the DC Bus voltage proved to give an adequate response, why this was applied when designing controllers.

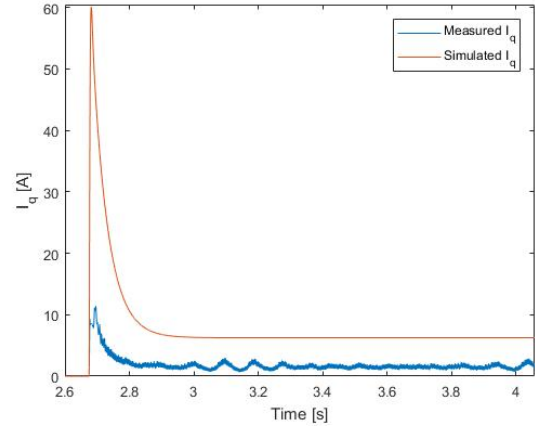


Fig. 14 Voltage step with current responses.

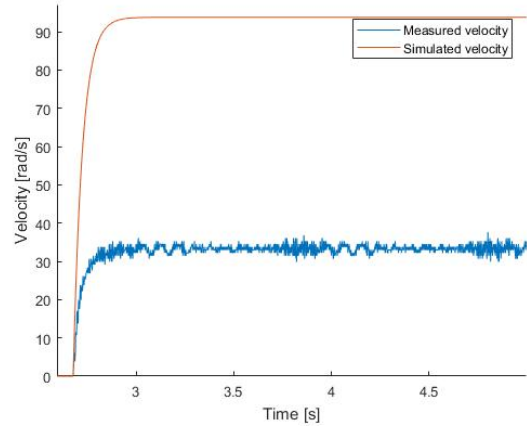


Fig. 15 Voltage step with current responses.

7. Control

As the couplings was considered disturbances and the linear model adequate for control design purposes, a root locus revealed a dominant pole and zero which was utilized to simplify the transfer function to:

$$G_{q,a} = \frac{K(s + \beta)}{\tau s + 1} \quad (20)$$

Where,

$$\begin{aligned} \tau &= 0.0372 \\ \beta &= 2.048 \\ K &= 17.886 \end{aligned}$$

A previously designed PI controller [6] gave an overshoot of 50 % but due to the maximum power output of the inverter, of 1.5kW, and the desire to minimise energy consumption, it was decided to design a controller with no overshoot. This was done

with Internal Model Control (IMC) which builds on the idea, of only feeding back model inaccuracies and disturbances. A schematic of the IMC approach is shown on Fig. 16.

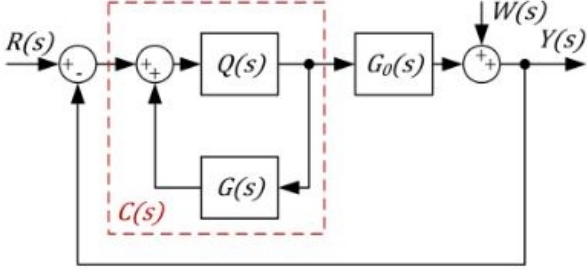


Fig. 16 Internal Model Control schematic from [9].

Descriptions of the used parameters can be found in Tab. II.

Parameter	Symbol
Real plant	$G_0(s)$
Modelled plant	$G(s)$
Compensator	$Q(s)$
Closed Compensator	$C(s)$
Disturbances	$W(s)$
Input	$R(s)$
Output	$Y(s)$

Tab. II Optimized parameters for the quarter car model..

The model G is separated as:

$$G = G_+ \cdot G_- \quad (21)$$

Where G_+ is chosen as:

$$G_+(s) = \frac{K\beta}{\tau s + 1} \quad (22)$$

A filter implemented to apprehend singularity of C . It is chosen as;

$$G_f = \frac{1}{\lambda s + 1} \quad (23)$$

The compensator is calculated as:

$$Q = (G_+)^{-1} \cdot G_f = \frac{\tau s + 1}{K\beta(\lambda s + 1)} \quad (24)$$

$$C(s) = \frac{Q}{1 - G_+Q} = \frac{\tau s + 1}{K(\beta\lambda - 1)s} \quad (25)$$

The compensator is thus a PI controller, with the PI coefficients:

$$K_p = \frac{\tau}{K(\beta\lambda - 1)} \quad , \quad K_i = \frac{1}{K(\beta\lambda - 1)} \quad (26)$$

This controller results in the closed loop system;

$$Y = \frac{G_0(\tau s + 1)}{K(\beta\lambda - 1)s + G_0(\tau s + 1)} R + \frac{K(\beta\lambda - 1)s}{K(\beta\lambda - 1)s + G_0(\tau s + 1)} W \quad (27)$$

As G_a gets closer to the real system G , the closed loop system becomes:

$$\lim_{G_a \rightarrow G_0} Y = \frac{\frac{1}{\beta}s + 1}{\lambda s + 1} R + \frac{(\lambda\beta - 1)s}{\beta(\lambda s + 1)} W \quad (28)$$

As s goes towards 0, the influence of the disturbance becomes zero, while the output Y becomes the reference value R .

Requirements for the controller is stated as:

$$\frac{1}{\beta} < \lambda \quad BW < 3,000 \frac{rad}{s} \quad BW > 1,500 \frac{rad}{s}$$

Where BW is the closed loop bandwidth. To meet these requirements, λ is chosen to be 0.55, which is found through bode plots. The controller is then tuned by increasing the the integrator gain, to decrease the rise time without creating an overshoot. The closed loop step response of the system with the old, the new and the tuned new controller is plotted and compared in Fig. 17.

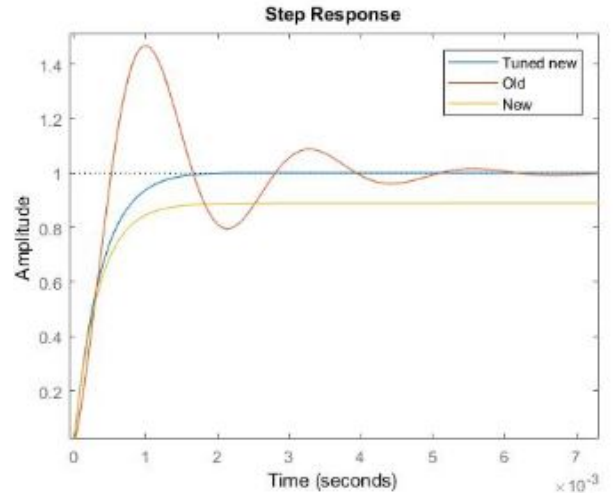


Fig. 17 Step response.

Even though it looks like the new controller without tuning have a steady state error, this is not the case, as it slowly moves to the desired value. The tuning has significantly improved the new controller, having decreased the rise time immensely without

any noticeable drawbacks. This tuned controller is also considered superior to the old controller, since it has no overshoot and a shorter settling time. The control design is thus considered a success. It is implemented in the real system, and a step of 2 amp is performed.

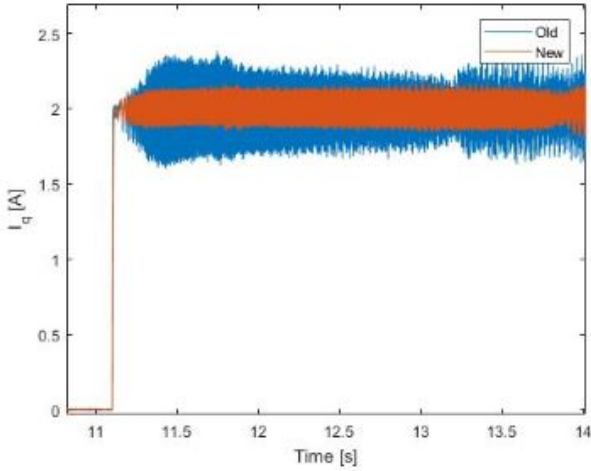


Fig. 18 Step response in real system.

The result of the test can be seen on Fig. 18. The old controller did not overshoot in this example, unlike previous real system test. It is assumed, that the reason for this, is due to a lower load torque in the newest test. The new controller still proved superior however, especially considering reduction of noise. This is because it is less aggressive near steady state, thus being less affected by noise and disturbances.

8. VTP model

A VTP model is made to simulate the suspension unit. It is modelled as a quarter car, with either a passive or a skyhook suspension control scheme.

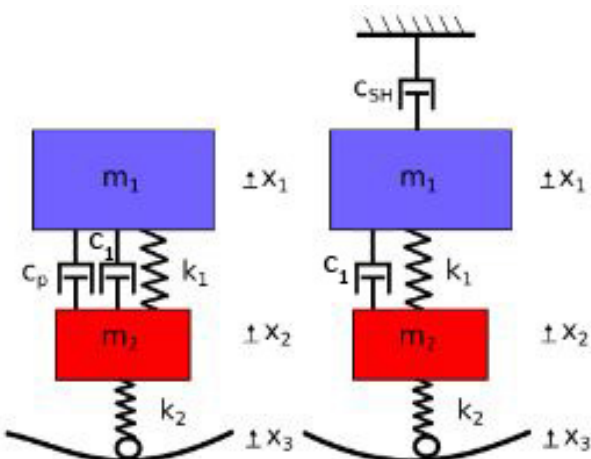


Fig. 19 Car model with passive (left) and skyhook (right)

Skyhook uses the idea of implementing a fictive damper between the suspended mass, m_1 and the sky. Due to limited access to the real VTP, an optimization algorithm based on data from a frequency sweep of the real system, was used to calculate model parameters, which is available in Tab. III.

Parameter	Symbol	Value	Unit
Body mass	m_1	698.5	[kg]
Wheel mass	m_2	69.9	[kg]
Suspension damper	c_1	$6.84 \cdot 10^3$	[Ns/m]
Suspension spring	k_1	$4.9 \cdot 10^6$	[N/m]
Tire spring	k_2	$5.89 \cdot 10^8$	[N/m]

Tab. III Optimized parameters for the quarter car model.

These parameters seems pretty high, but are still deemed realistic. The model is then used to simulate the passive suspension versus the skyhook. It simulated the vehicle driving over a roadbump at 10km/h. The acceleration response of chassis can be seen on Fig. 20.

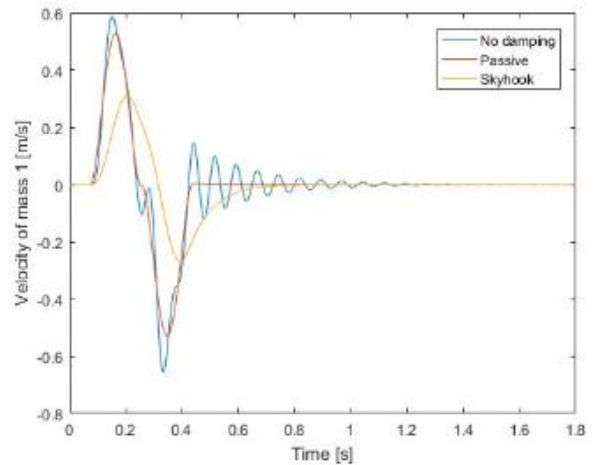


Fig. 20 Acceleration response of chassis

This shows the advantage of skyhook, however it also required more power from the PMSM. Due to this huge power demand, a passive suspension system is recommended for this VTP.



Fig. 21 Load motor (left), torque transducer (center) and PMSM (right).

A passive damper was tested on the PMSM on a test bench, see Fig.21 where opposing motor was running with a sinusoidal velocity trajectory, and the PMSM was dampening it with different damping coefficients. The torque output was measured versus the reference torque, see Fig. 22.

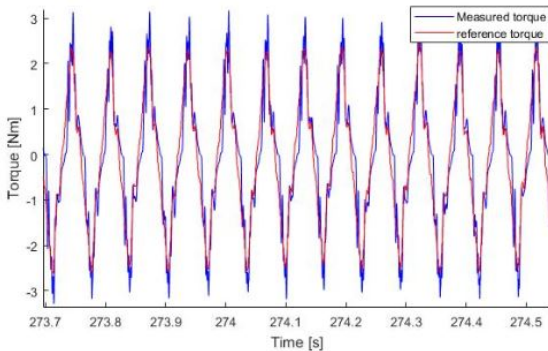


Fig. 22 Torque response

The motor followed the torque reference at all frequencies, with highest measured being 15Hz. This test concluded that the FOC control for the PMSM was adequate for high frequency torque trajectories, i.e. it is suitable for passive suspension usage.

9. Conclusion

This paper has investigated the design and concept of an electromagnetic shock absorber developed by Aalborg University. This included manufacturing the PMSM and MLS, which provided a deeper understanding of the system. Starting out with the governing equations, a nonlinear model was established. Hereafter, a series of test has been carried out to determine the parameters required for this model. This resulted in values for phase resistance, phase inductance, back-EMF constant, torque constant, friction and iron losses.

Open loop simulations was carried out with the obtained parameters and subsequently compared with test data acquired from the experimental setup. Unfortunately, the results proved unsatisfactory. The same study was executed with closed loop control instead. This provided better results as the transient responses matched.

In spite of deviations, a linear model has been derived using Taylor series approximations on non-linear expressions in the governing equations. A controller has been designed from the internal model

control principle. Subsequent tests of this has proven the design holds in a test environment. The controller has been compared with a previously designed controller, and the overshoot has been reduced fulfilling the design goal. Investigations into the vehicle dynamics suggest the PMSM is suitable for use in a suspension system.

Acknowledgement The authors of this work gratefully acknowledge Sintex for sponsoring the 5th MechMan symposium.

References

- [1] GMAuthority, “*General Motors Magnetic Ride Control Technology*,” 2014. Available: <http://gmauthority.com>.
- [2] Micro-tronik, “*Mercedes Benz 216 Suspension system Control Unit*,” 2004. Available: <http://www.micro-tronik.com>.
- [3] T. C. Connection, “*Bose Unveils "Project Sound"*,” 2004. Available: <http://www.thecarconnection.com>.
- [4] N. Berg, R. Holm, and P. Rasmussen, “*Theoretical and Experimental Loss and Efficiency Studies of a Magnetic Lead Screw*,” *IEEE Trans. on Industry Application*, 2015.
- [5] N. Berg, R. Holm, M. Walkusch, P. Rasmussen, and R. Hansen, “*Design of a Magnetic Lead Screw for Wave Energy Conversion*,” *IEEE Trans. on Industry Application*, 2013.
- [6] N. Berg, “*Active Suspension - WPI&2*,” tech. rep., Aalborg University, 2016.
- [7] L. Mathe and P. O. Rasmussen, “*AC Motor Drives: Converters and Control*,” 2017. [Course].
- [8] W. Soong, “*Inductance Measurements for Synchronous Machines*,” *Power Engineering Briefing Note Series*, 2008.
- [9] L. Schmidt and P. Johansen, “*Multi variable and non-linear control methods*,” 2017. [Course].